Reprinted from
2013 IEEE Transactions on Microwave Theory and Techniques
Volume 61, Issue 5

IR-UWB Radar Demonstrator for Ultra-Fine Movement Detection and Vital-Sign Monitoring

Bernd Schleicher, *Member, IEEE*, Ismail Nasr, *Student Member, IEEE*, Andreas Trasser, and Hermann Schumacher, *Member, IEEE*

***Abstract*—In this paper an impulse-radio ultra-wideband (IR-UWB) hardware demonstrator is presented, which can be used as a radar sensor for highly precise object tracking and breath-rate sensing. The hardware consists of an impulse generator integrated circuit (IC) in the transmitter and a correlator IC with an integrating baseband circuit as correlation receiver. The radiated impulse is close to a fifth Gaussian derivative impulse with $\sigma = 51$ ps, efficiently using the Federal Communications Commission indoor mask. A detailed evaluation of the hardware is given. For the tracking, an impulse train is radiated by the transmitter, and the reflections of objects in front of the sensor are collected by the receiver. With the reflected signals, a continuous hardware correlation is computed by a sweeping impulse correlation. The correlation is applied to avoid sampling of the RF impulse with picosecond precision. To localize objects precisely in front of the sensor, three impulse tracking methods are compared: Tracking of the maximum impulse peak, tracking of the impulse slope, and a slope-to-slope tracking of the object's reflection and the signal of the static direct coupling between transmit and receive antenna; the slope-to-slope tracking showing the best performance. The precision of the sensor is shown by a measurement with a metal plate of 1-mm sinusoidal deviation, which is clearly resolved. Further measurements verify the use of the demonstrated principle as a breathing sensor. The breathing signals of male humans and a seven-week-old infant are presented, qualifying the IR-UWB radar principle as a useful tool for breath-rate determination.**

***Index Terms*—Medical applications, medical imaging, ultra-wideband (UWB) circuit techniques, UWB communications, UWB signals generation and transmission.**

I. Introduction

FROM 1998 to 2010, an average number of 37 children died every year in the U.S. due to hyperthermia when being left unattended in a car [1]. Interestingly, about half of the children were left in the car unintentionally while sleeping. In addition, it is estimated that each year hundreds of children experience heat illnesses by the same cause. As found out experimentally by [1], a relatively moderate ambient temperature of 22 °C (73 °F) can drive the temperature in a car up to 47 °C (117 °F) within 60 min on a sunny day. An automatic mechanism (car seat occupancy detection) could remind the driver of the child. Some detection techniques have certain disadvantages: a pressure sensor in the seat, for example, cannot distinguish between a child and a heavy bag, an acceleration sensor will not respond when the child is asleep, and a thermal sensor will not detect a person when the ambient temperature is around 37 °C (100 °F). To avoid discomfort for the child, a wireless detection could be of interest. For this reason an impulse-radio ultra-wideband (IR-UWB) sensor is proposed as a breathing-pattern detector, and the suitability of this technology is investigated by a demonstrator. Additionally, such a radar system could be used in a variety of other applications, for example, for breath-rate measurements on adults, children, or newborns in a clinical intensive care unit. In contrast to the method using wired electrodes, this sensor would have the advantage of measuring the breath rate contact free, which would increase the acceptance by patients or parents. It could be pre-installed in the intensive care unit, avoiding the need for aligning electrodes and improving hygiene, because the patient must not be touched.

According to the definition of the U.S. Federal Communications Commission (FCC), a signal is ultra-wideband (UWB) when its fractional bandwidth is larger than 25% or the absolute bandwidth larger than 500 MHz [2]. The FCC regulation allows a coexistence of UWB radiation with present radio services, but to minimize interference with them, UWB systems must operate at a very reduced mean effective isotropic radiated power (EIRP) density level of -41.3 dBm/MHz. To further protect existing sensitive services, e.g., GPS or radio astronomy bands, the FCC introduced frequency masks for UWB emission. For indoor and outdoor UWB operation, the FCC allows a density level of -41.3 dBm/MHz only below 960 MHz or in the range from 3.1 to 10.6 GHz. For other frequencies, stricter regulations apply, as can be seen in [2].

Besides its license-free use, IR-UWB technology offers interesting features for modern sensing systems. In contrast to continuous wave (CW) systems, it enables radiation of short time-domain transients, which allow the use of new and very simple system concepts for precise radar devices. An interesting aspect of impulse transmission is the strong power-saving potential because large parts of the electronics in the transmitter and receiver are not used between impulses and can therefore

Manuscript received October 13, 2012; revised February 16, 2013; accepted February 21, 2013. Date of publication March 26, 2013; date of current version May 02, 2013. This work was supported by the German Research Foundation (DFG) under the framework of the priority program UKoLoS.

B. Schleicher was with the Institute of Electron Devices and Circuits, Ulm University, 89081 Ulm, Germany. He is now with TriQuint Semiconductor, 81829 Munich, Germany (e-mail: bernd.schleicher@tqs.com).

I. Nasr was with the Institute of Electron Devices and Circuits, Ulm University, 89081 Ulm, Germany. He is now with Friedrich-Alexander-University, 91058 Erlangen, Germany.

A. Trasser and H. Schumacher are with the Institute of Electron Devices and Circuits, Ulm University, 89081 Ulm, Germany (e-mail: hermann.schumacher@uni-ulm.de).

Color versions of one or more of the figures in this paper are available online at http://ieeexplore.ieee.org.

Digital Object Identifier 10.1109/TMTT.2013.2252185

operate in idle state. This leads to a small duty cycle and therefore to a huge saving potential. A further general benefit of UWB is the spreading of the transmittable signal across a large spectrum, necessary to obtain a low transmit power density. Electromagnetic disturbance of the IR-UWB system to nearby electronic devices is mediated much more than in conventional narrowband radio systems. Therefore, the use of UWB technology is well suited for electromagnetically critical environments, e.g., clinics.

The idea behind medical diagnostics using electromagnetic emissions is to use the impulse reflections at the tissue boundaries of the person under test. For breathing, the movement of the chest is determined. Reflections arise due to the different dielectric properties of the tissue penetrated. The amount of electromagnetic amplitude reflection at the air–skin boundary is about 72%. A further contribution to the reflected impulse energy comes from the part of the impulse energy penetrating the skin and being reflected at a next tissue boundary.

Measuring the breath-rate with impulse-radio technology was first introduced by McEwan in [3]. He applied an impulse generator (IPG) emitting in the lower part (<960 MHz) of the UWB spectrum. With the release of the FCC UWB regulations, IR-UWB systems for breath-rate detection were built, applying higher operating frequencies. Systems with compliance to the FCC masks are, for example, shown by [4], which uses a self-built IPG based on a step recovery diode (SRD), making use of the lower part (3.1–6 GHz) of the UWB regulation. In [5], a commercial IPG unit is used, emitting in the middle (4–7.5 GHz) of the FCC UWB spectrum, and [6], which uses a commercial IPG unit as well, addressing a frequency range from 3.1 to 8 GHz within the UWB allocation. Besides impulse generation, recently shown IR-UWB breath-rate sensors differ by their concept transforming the impulse from analog RF domain into data for post-processing. Mainly two impulse processing concepts for acquisition of the RF impulse can be found in the literature. One applies a direct sampling of the impulse in the RF domain, either by real-time sampling [5], [7] or under sampling [6], [8]–[10], both using powerful real-time or equivalent-time sampling oscilloscopes. The other concept applies a cross-correlation detection to convert the impulse to a low-frequency equivalent [4], [11], where it can be digitized at much lower sampling rates.

In this paper, an implementation in compliance with the FCC-allocated UWB mask is presented, making efficient use of the complete mask. A cross-correlation concept is applied, using custom-designed UWB integrated circuits (ICs) in the transmitter and receiver branch, mounted together with commercial components on a compact antenna substrate. A demonstrator is proposed and its operation and sensing precision verified by measurements. Breath-rate measurements on two male humans and an infant are shown.

II. Principle of Operation

The method used in this approach is the principle of sweeping impulse correlation, similar to a concept in [12]. The system implementation can be seen in the block diagram of Fig. 1. By this method, an impulse train, consisting of short time-domain UWB

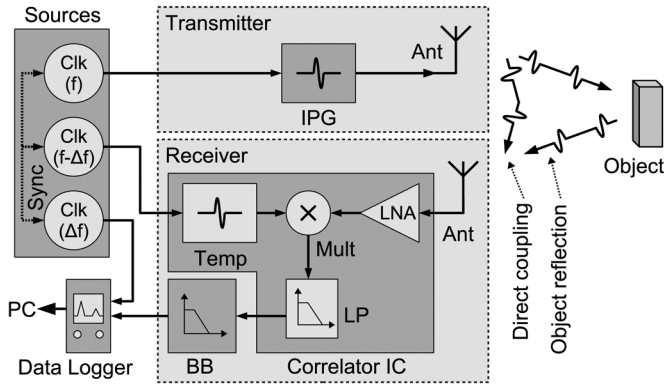

Fig. 1. Block diagram of the correlation-based radar demonstrator.

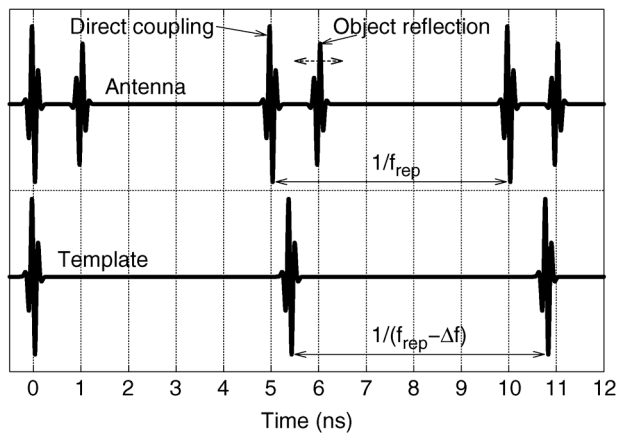

Fig. 2. Antenna receive and the template signal, sweeping through the receiver channel (Δf not to scale).

impulses, is continuously radiated by the IPG of the transmitter at repetition rate f. The transmitted impulse train approaches the object placed in front of the radiation arrangement and is reflected back to the receiver. Due to the applied bistatic radar concept, an impulse of the direct coupling between the antennas will also approach the receiver; it will arrive earlier than the reflected impulses because of the shorter distance between the antennas. In the receiver, the arriving impulse signals are first amplified by a low-noise amplifier (LNA) and further processed by a hardware correlation operation using a template impulse generator (Temp), a broadband four-quadrant multiplier (Mult), and two integrating filter stages (low-pass (LP) filter and baseband (BB) circuit).

The idea behind using the sweeping correlation concept is to apply a small frequency difference to the template impulse train in the correlation receiver, resulting in a repetition frequency $(f - \Delta f)$ of the template impulse train. With this, the template impulse is continuously sweeping with respect to the received impulse train. This behavior can be seen in Fig. 2, where the upper part represents the received impulse train with static direct coupling and reflection at the object, and the lower part represents the template impulse sequence.

While the template impulse train is sweeping, the correlation (i.e., multiplication and integration) of the complete channel is continuously and repetitively generated in the correlation receiver. The correlation of the received signal can be seen in the

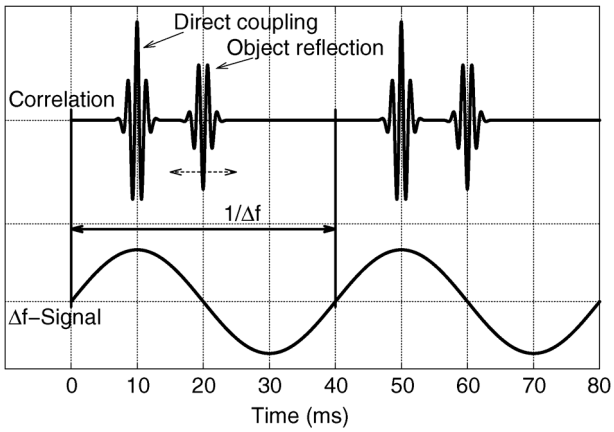

Fig. 3. Correlator output signal showing the static direct coupling and a reflection at the object, together with a generated Δf-signal used to separate the continuous correlation sweep.

upper part of Fig. 3. The advantage of using the hardware correlation principle is that the impulses do not have to be sampled at a sampling rate in the picosecond range, but at a more adequate sampling rate, depending on the frequency difference Δf (here: microseconds).

The lower part of Fig. 3 shows a sinusoidal signal of the frequency difference Δf (see Fig. 1), which has the same cycle period as the correlation signal and is used to separate the correlation sequences. This is done by cutting the sequence at every zero crossing of the Δf-signal. By the separation of the correlation sequence, a fixed time instance is generated, which allows to determine the time distance $T_{\rm ob}$ of the object from the antennas. With $T_{\rm ob}$, the absolute position of the object $d_{\rm ob}$ can be calculated by

$$d_{\rm ob} = \frac{c_0}{2 \cdot f} \cdot T_{\rm ob} \cdot \Delta f \tag{1}$$

with f being the repetition frequency of the transmit impulses, Δf being the repetition rate difference between transmitter and receiver repetition rates, and c_0 being the speed of light. The 1/2 is due to the impulse traveling the distance between the object and antennas twice. In case the object is moving, the reflected impulse and the corresponding correlation impulse will change its time-domain location with respect to the zero crossing of the Δf-signal and the movement can be computed.

The chosen parameters f and Δf have an impact on the system performance. For the built demonstrator, a repetition frequency $f = 200$ MHz and $\Delta f = 25$ Hz is applied. The correlator output signal and the Δf-signal are continuously sampled by a data logger with a sampling time $T_s = 30$ μs. For these parameters, the system performance can be calculated. The maximum distance of sensing $d_{\max}$, where a reflected impulse does not overlap with the impulse in front, can be calculated by

$$d_{\max} = \frac{c_0}{2 \cdot f}. \tag{2}$$

Using $f = 200$ MHz, we obtain $d_{\max} = 0.75$ m, which is suitable for the intended application scenarios. The highest observation frequency $f_{\max}$ of the moving object in the presented setup can be calculated by

$$f_{\max} = \frac{\Delta f}{2}. \tag{3}$$

With the chosen values, a maximum sinusoidal movement of an object of $f_{\max} = 12.5$ Hz can be resolved, which is well suited to the slowly moving breath rate. The correlation signal is sampled at quantized time steps by the data logger. Therefore, the point-to-point time resolution is quantized by the difference between two sampling instances. For the system, a point-to-point resolution $d_{\rm min,pp}$ can be calculated using (1) and replacing $T_{\rm ob}$ by the sampling rate of the data logger T_s, which leads to a minimum point-to-point resolution $d_{\rm min,pp} = 0.56$ mm when applying the above values. Mathematical methods to improve the resolution are shown in a later section. Using this system principle and the chosen parameters, a hardware demonstrator is built.

III. Hardware Implementation

In this section, the applied circuits are presented for use in the IR-UWB radar system. The designed ICs are fabricated in an Si/SiGe heterojunction bipolar transistor (HBT) technology with a relaxed 0.8-μm minimum drawn feature size by Telefunken Semiconductors [13]. The monolithic microwave integrated circuits (MMICs) are directly connected to the feeding line of Vivaldi-type transmit antennas to avoid connector-induced reflections at discontinuities on the line. The MMICs and the antenna design were available from collaboration projects. The Vivaldi antennas consist of an exponentially tapered slot line and a transition to a microstrip line by a Marchand balun, as presented in [14], and are chosen for their broadband behavior. The maximal gain of the antenna is 9.3 dBi, the gain at 3.1 GHz is 3 dBi. More details on the antenna can be found in [11] and [15]. The circuit boards, including the antennas and the used circuits, are fabricated on a 0.51-mm-thick RO 4003 substrate.

A. Impulse Transmitter for the FCC Indoor Mask

The IPG circuit has an important role with regard to the compliance with the allocated UWB masks. In the literature, a variety of impulse shapes have been proposed for use with the FCC masks. In this work, an impulse close to a fifth derivative of a Gaussian bell shape with a standard deviation of $\sigma = 51$ ps is targeted, as introduced by [16]. This theoretical impulse shape fills the FCC indoor mask nicely and at the same time has a very short time-domain extension of 180-ps measured full-width at half maximum (FWHM).

A block diagram of the circuit that generates such a waveform can be seen in Fig. 4. The applied IPG was available from [17] and [18]. It consists of three main subcircuits. The first subcircuit is a two-stage limiting amplifier. It is fed by the slope of an input control signal and is used to convert the input signal from a potentially long rise-time signal into a rectangular signal with a short rise time. The circuit can be operated as well by a sinusoidal. The rising slope of the rectangular signal is differentiated by the spike generation subcircuit, which forms a short-width Gaussian-like output spike. The corresponding negative spike,

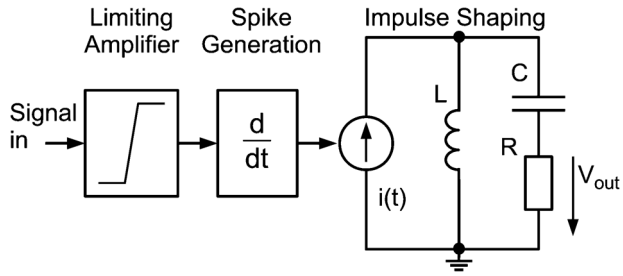

Fig. 4. Simplified circuit schematic of the applied IPG IC.

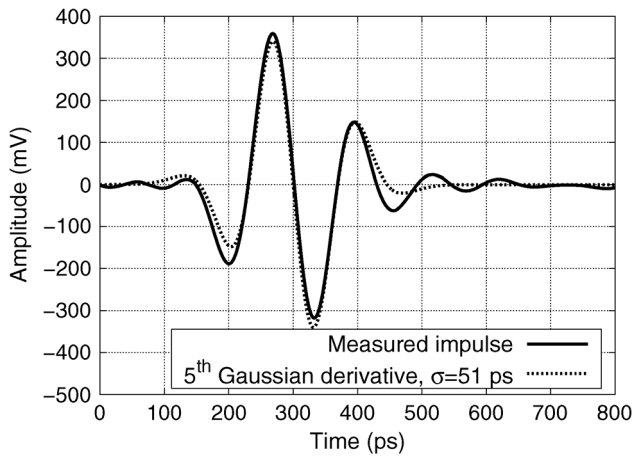

Fig. 5. Time-domain measurements of the FCC-compliant IPG IC.

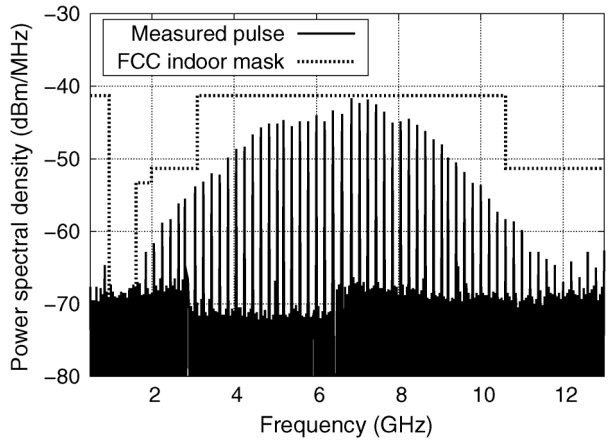

Fig. 6. Spectral-domain measurements of the FCC-compliant IPG IC.

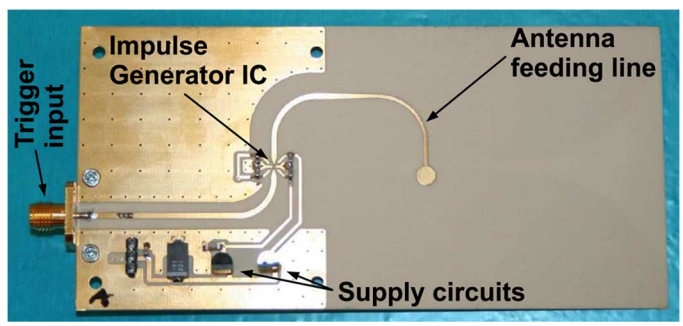

Fig. 7. Photograph of the compact impulse transmitter. Antenna radiation structure on backside.

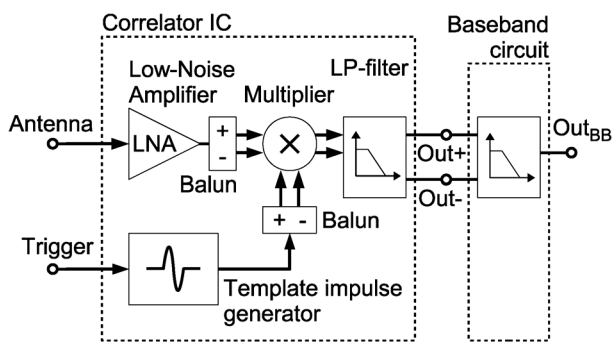

Fig. 8. Block diagram of the applied hardware correlation receiver.

coming from the falling slope of the rectangular signal, is suppressed. In the third subcircuit, the impulse forming takes place. The Gaussian-like spike activates a transistor, where a current spike $i(t)$ is excited to an under damped LC resonator. At the output, a transient voltage impulse $v_{\rm out}$ is formed at the system impedance $R = 50\ \Omega$, which is very similar to a fifth Gaussian derivative with $\sigma = 51$ ps.

The measured on-chip output impulse in the time domain can be seen in Fig. 5 in comparison to an ideal fifth Gaussian derivative, showing the close fit to the waveform. The measured on-chip output signal in spectral domain is given in Fig. 6, proving the efficient use of the FCC UWB frequency allocation for indoor applications. For this measurement, a sinusoidal input control signal of 200 MHz was chosen, which results in a measured line spectrum with a frequency difference of 200 MHz between the lines.

Packaging of the MMIC is done by chip-on-board mounting on the antenna substrate, as can be seen in Fig. 7. The bond wires have a negligible influence on the impulse shape. A radiation of the impulse via two antennas shows a changed impulse form at the output of a receive antenna, when viewed on an oscilloscope. This radiated impulse can be fitted to a seventh Gaussian derivative with $\sigma = 65$ ps. The change in impulse shape is due to the bandpass characteristic of the antennas, suppressing the impulse shape at the edges of the spectrum, and therefore broadening the impulse shape in the time domain. Measurements of this behavior can be seen in [15]. However, the changed impulse shape has only a minor influence on the correlation operation because the impulse shapes of fifth and seventh Gaussian derivative with their corresponding σ's have very similar time-domain properties.

B. Hardware Correlation Receiver

A hardware correlation receiver is built for use of the cross-correlation operation with two impulses. The complete receiver combines an FCC-compliant correlator IC with a BB circuit and is mounted on the foot point of the receiving Vivaldi antenna. A block diagram of the complete correlation receiver can be seen in Fig. 8.

The correlator MMIC was available from [19]. It consists of an LNA, a template IPG, a multiplier, and a first integrating LP filter. The template IPG is the same as the FCC-compliant fifth

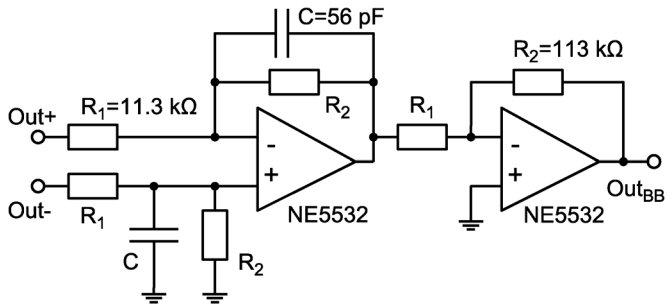

Fig. 9. Simplified schematic of the BB circuit using two operational amplifiers.

Gaussian derivative IPG, shown in Section III-A. The UWB LNA consists of a three-stage design, using interstage and stage-to-stage feedback for gain flatness and broadband noise matching at the same time. It features a 23-dB flat gain response and a state-of-the-art noise figure of 2.8 dB in the middle of the 3.1–10.6-GHz band. A detailed evaluation of the separately characterized LNA can be found in [20]. For the multiplication operation, a four-quadrant fully balanced Gilbert-cell multiplier is applied and converters (baluns) are placed at the input for a conversion of the single-ended LNA and template IPG signals to the differential inputs of the Gilbert-cell multiplier. The multiplier's differential output is filtered by a first integrating on-chip low-pass filter with a cutoff frequency of around 900 MHz. A detailed evaluation of the correlator IC can be found in [19].

At the output of the correlator IC, a BB circuit is externally connected, which provides a conversion from differential to single ended, amplifies the output signals, and applies further integration by a strong LP filtering. The applied circuit topology, which provides all three operations, can be seen in Fig. 9. It is based on a differential amplifier using NE5332 operational amplifiers, enhanced by single-pole LP filters in both branches. Due to its high input impedance, the BB circuit can operate dc coupled to the correlator IC and therefore does not detune the IC's internal biasing. A second gain stage is cascaded. The voltage gain of each stage is set by $G_V = R_2/R_1 = 10$ and the LP-filter's 3-dB corner frequency is adjusted to $f_{LP} = 1/(2\pi \cdot R_2 \cdot C) = 25$ kHz.

The correlation receiver IC and the BB circuit contains all building blocks necessary for a correlation receiver. For the correlation receiver, a packaging is done as well, integrating the IC and BB circuit in a compact arrangement on the receiving antenna substrate. A photograph of the correlation receiver antenna can be seen in Fig. 11. To show the correlation operation, a measurement is performed using a subversion of the receiver with connector at the antenna input. At this input, an IPG is connected to the correlation receiver, attenuated by 30 dB. A varying time delay τ between the impulses is performed by a changing phase shift between the two triggering signal sources, which is similar to the sweeping correlation operation applied in the demonstrator. The corresponding voltage output signal $\mathrm{Out_{BB}}$ is monitored, which results in the computed correlation of the antenna signal with the template impulse. The measured normalized correlation can be seen in Fig. 10, where it is compared to an ideal correlation of fifth Gaussian derivatives. The curve shows a clear correlation maximum and can therefore be

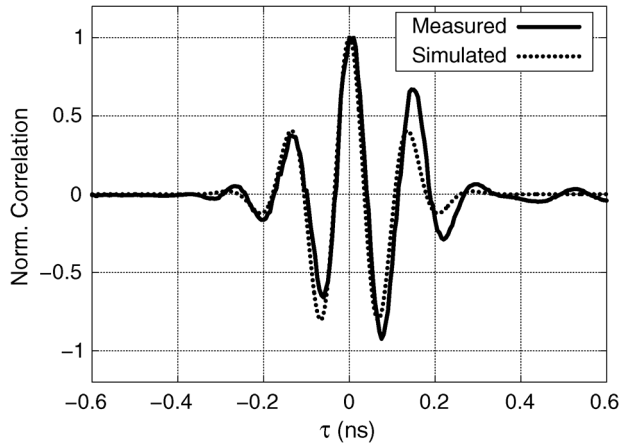

Fig. 10. Measured correlation of the receiver arrangement, compared to an ideal correlation curve.

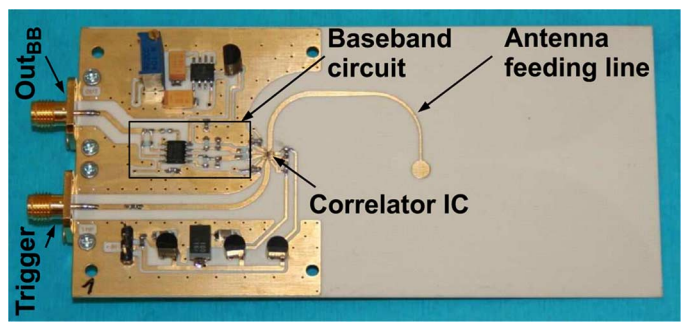

Fig. 11. Photograph of the compact correlation receiver. Antenna radiation structure on backside.

used for the intended sensor. The deviation from the ideal impulse shape is due to the varying group delay in the multiplier and reflections at interface boundaries of the externally connected IPG.

C. Control and Sampling Circuitry

As indicated in the block diagram in Fig. 1, the IPGs in the transmitter and receiver are fed by sinusoidal signals coming from three signal sources. To obtain stable frequency differences, all sources need to be synchronized among each other. A direct digital synthesizer (DDS) signal source AD9959 [21] is used for this purpose, which is available as an evaluation board version [22]. The board has four channels (three are used) that can be controlled individually in frequency and phase, and share a common synchronization reference. Two channels supply the transmit and receive boards with frequencies of f and $(f-\Delta f)$, respectively, the third is used for the Δf signal as a synchronization signal to the data logger. The output frequency of the AD9959 ranges from 0 to ∼210 MHz with a minimum step size of ∼0.116 Hz, the minimum adjustable phase step is ∼ 0.019°. The nondecimal fractions of the values are due to the binary operation of the device. A major concern is the sinusoidal purity of the controlling frequencies. For the DDS especially, nonharmonic spurs are identified as a major cause of amplitude jitter. The sinusoidal output contains spurs up to a spurious-free dynamic range (SFDR) of 50 dBc. When using the sinusoidal as a triger signal to the IPGs, this amplitude jitter will lead to a cycle-to-cycle jitter in the generated impulse train and will have

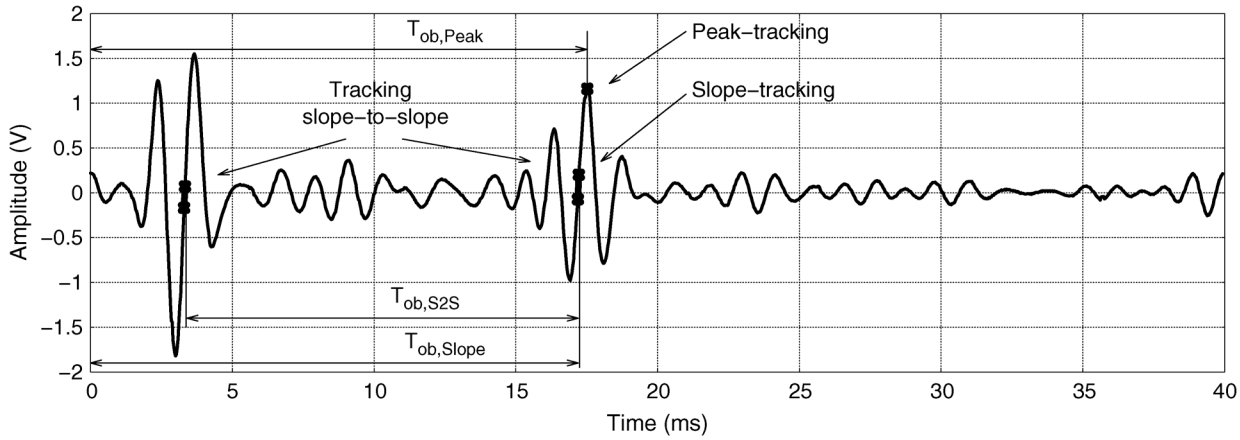

Fig. 12. Measured correlation sweep, showing a signal of the direct coupling and a reflection at the metal plate. Additionally the three tested methods for object tracking are illustrated in the plot.

significant impact on measurement precision. The jitter variation Δt of a sinusoidal signal due to an overlaying nonharmonic spur signal can be estimated using the change in time deviation of the sinusoidal zero crossing and $\sin(x) \approx x$ for small values of x as

$$\Delta t = 2 \cdot \frac{\mathrm{SFDR}}{2\pi \cdot f} \tag{4}$$

where f is the frequency of the sinusoidal signal. Calculating this for an SFDR of 50 dBc and $f = 200$ MHz, we obtain a jitter variation $\Delta t = 5$ ps, which is large for a precise ranging, compared to the 180-ps (FWHM) impulse width of the fifth Gaussian derivative. Pure output sinusoidal control signals are obtained by bandpass filtering. To sufficiently suppress spurs that are very close to the wanted sinusoidal, a filter with a small passband is necessary. Therefore, helix bandpass filters are built, as described in [23] and [24], having an insertion loss of 0.9 dB at 200-MHz center frequency and a 3-dB bandwidth of 6 MHz. The SFDR reaches a value larger than 70 dBc, which results in a jitter variation $\Delta t < 0.5$ ps.

The Δf signal as the third signal of the DDS board is also purified, but due to its low frequency, this is done by software after sampling. There the Δf signal is first smoothed with a moving average algorithm; after this, the number of zero crossings in a time interval are counted. By this, a precise frequency of the sinusoidal signal can be obtained and a phase correct pure sinusoidal is constructed, which is applied for the precise separation of the correlation repetition.

For data acquisition, a USB oscilloscope [25] in the data logger mode is used, which transfers the sampled data with $T_s = 30\ \mu$s sampling time to a personal computer. For control of the DDS board frequencies and post-processing of the acquired measurement data, a custom computer program is written using LabWindows/CVI from National Instruments [26], which is a C-based programming software with prebuilt mathematical and graphical functions.

IV. Measurements Using the Hardware Correlator

A. Movement Detection Methods

After connecting the hardware, measurements of the demonstrator's operation are performed. First, an aluminium plate of 12×15 cm^2 is placed at a distance of 33 cm in front of the antenna arrangement. A measurement of one correlation sweep with an impulse of the direct antenna coupling and one reflection at the metal plate can be seen in Fig. 12. The object signal is clearly visible. The ringing after the two impulses is caused by the impulse response of the antennas. Three different methods of a precise location determination and movement extraction are compared in this arrangement by accurately calculating the time instance T_{ob} in (1) of the object from the continuously changing correlation plot. The comparison of methods is done with the metal plate placed in front of the demonstrator, which is not moving. The acquired metal plate positions are plotted in a histogram; the method with the smallest distribution error, and therefore, performing best, can be identified by the histogram distribution extension. All three tested methods are illustrated in the correlation plot of Fig. 12.

The first method is a simple tracking of the maximum peak of the object reflection signal. $T_{\mathrm{ob,Peak}}$ is taken in (1). A histogram of the tracking of the reflection peak is given in Fig. 13. It can be seen that the distribution is quantized with a step of the calculated 0.56 mm, resulting from the chosen system settings. The distribution width of the histogram is approximately 1 mm (FWHM).

The second method applies a tracking of the slope of the correlation signal. Therefore, a positive and negative sampling point around the zero-crossing next to the object reflection maximum is used to span a straight line (see Fig. 12). The point where the straight line crosses the zero axis is taken as time instance $T_{\mathrm{ob,Slope}}$. The constant error due to the time difference to the maximum peak is corrected by a calibration. In Fig. 14, the distribution of the slope tracking method can be seen. It becomes clear that the distribution is continuous because the zero-crossing of the slope does not depend on the quantized sampling instances, but the distribution width remains approximately the same as with the peak tracking method.

The third method tracks the slope of the reflection signal as in method 2, but additionally tracks the slope of the static impulse from the direct coupling. For the direct coupled impulse, a straight line is also spanned and the time instance of the second zero crossing is determined (see again Fig. 12). The difference

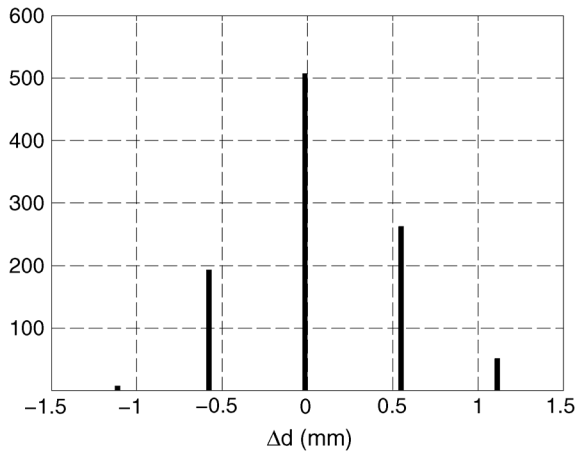

Fig. 13. Histogram distribution of the method tracking the maximum peak using $T_{\mathrm{ob,Peak}}$.

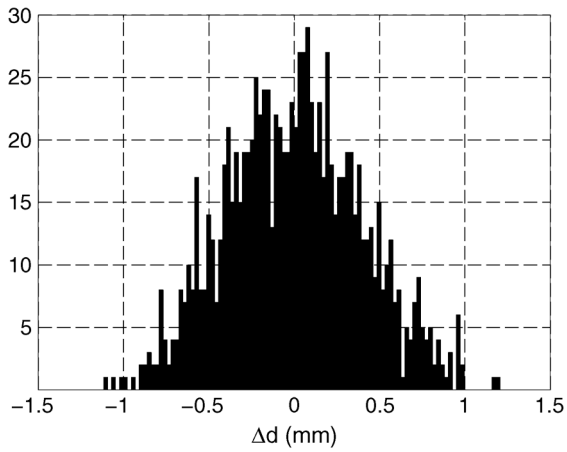

Fig. 14. Histogram distribution of the method tracking the slope using $T_{\mathrm{ob,Slope}}$.

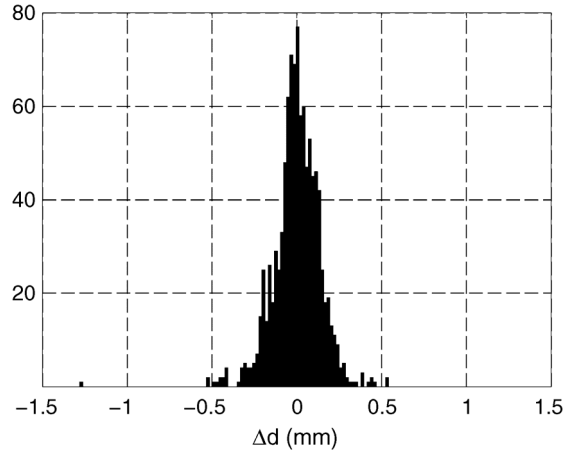

Fig. 15. Histogram distribution of the slope-to-slope tracking method using $T_{\mathrm{ob},S2S}$.

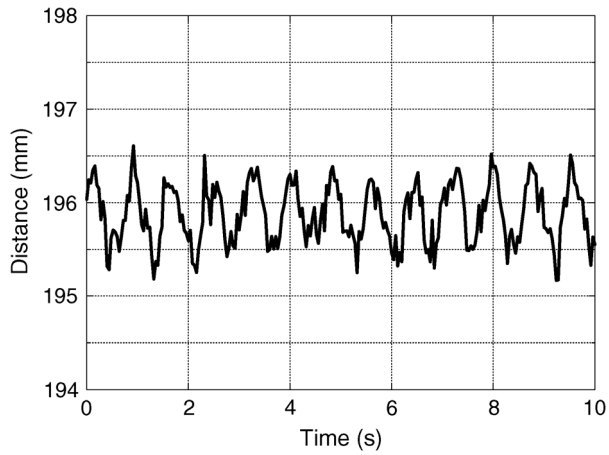

Fig. 16. Moving metal plate with a deviation of 1 mm at a mean distance of 19.6 cm in time domain.

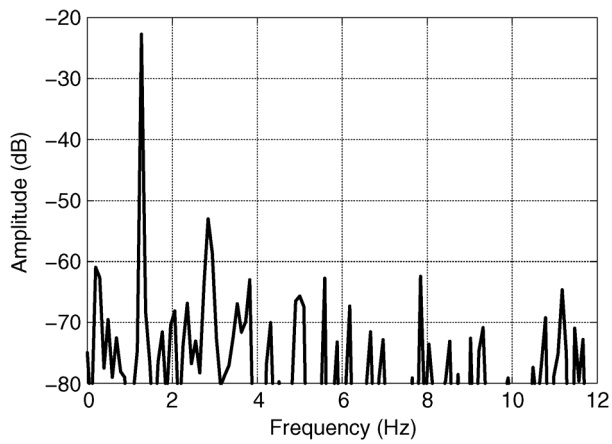

Fig. 17. Moving metal plate with a deviation of 1 mm in spectral domain.

of the two time instances $T_{\mathrm{ob},S2S}$ is used. Fig. 15 shows the histogram of this method. It is obvious that the distribution is continuous and that the distribution width has reduced to below 0.5 mm (FWHM). This is because the third method also removes the digit error due to the sampling of the Δf signal. The slope-to-slope tracking method performs best and is chosen for the further measurements.

B. Precise Movement Determination and Breath-Rate Sensing

Now, the aluminium plate is placed in front of the sensor for a precision movement measurement. The plate is mounted on a lever, which is moved by a rotation sledge. This results in a sinusoidal forward and backward movement of the metal plate. It is placed at a mean distance of $\sim$20 cm with a deviation of 1 mm and a rotation speed of 1.3 Hz. The movement measurement in time domain is given in Fig. 16. The location of 19.6 cm and the deviation of 1 mm can be clearly distinguished.

The corresponding spectral-domain signal, converted from the time signal by a Fourier transform, is given in Fig. 17. Here the spectral line with a frequency of 1.3 Hz can be determined with an amplitude of 30 dB better than the system noise floor.

In further measurements, male test persons, lying on the back, are placed in front of the sensor.[1] The sensor is mounted on a tripod and the sensor's radiation is pointed at the persons'

[1]The breath-rate measurements were approved by the ethic commission at Ulm University prior to the investigations.

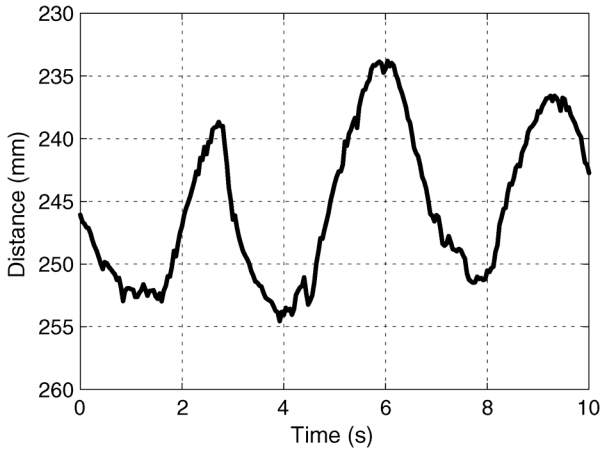

Fig. 18. Example obtained from a male test person breathing normally.

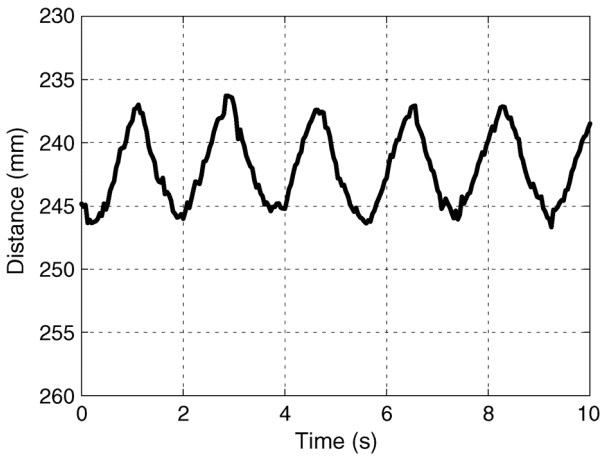

Fig. 19. Examples obtained from a male test person breathing artificially fast and flat.

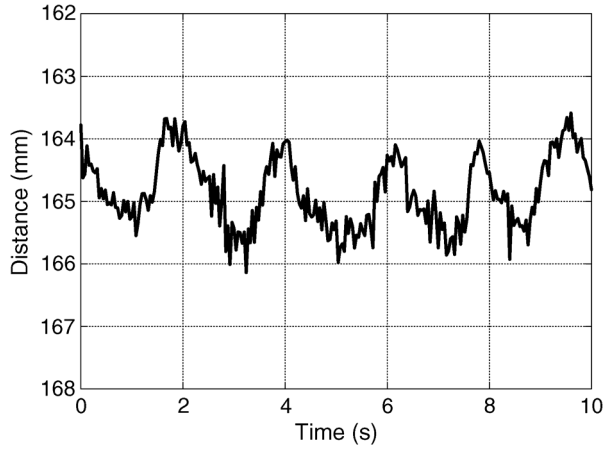

Fig. 20. Time-domain breathing cycle of a seven-week-old sleeping infant, showing a sequence with a continuous breathing cycle.

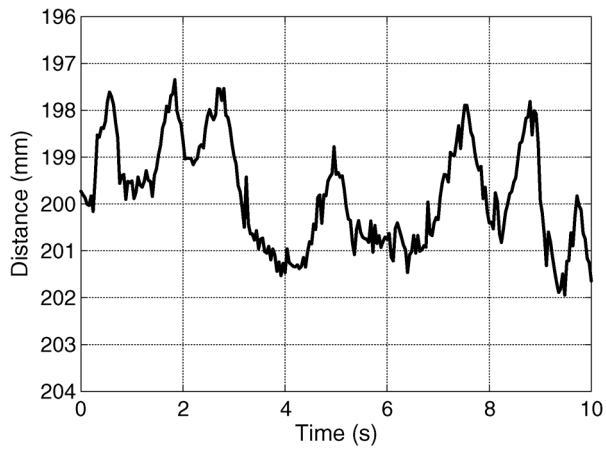

Fig. 21. Time-domain breathing cycle of the infant sleeping in a car seat, showing a sequence with a typically arrhythmic breathing of infants.

abdomen since this is the area of the largest breathing deviation. The radar cross section of a person's abdomen is different from the plane metal plate. As mentioned before, the reflection coefficient of tissue is different, but additionally the individual body shape of the person will have an influence on the reflected impulse. Therefore, the impulse, approaching the receiver may be slightly deformed. However, a slightly deformed reflected signal can be computed as well with the above-mentioned method, and it was found that the signals can be detected well. Note that the spectral location of the impulse is not changed by the tissue, so the compliance to the mask remains. Fig. 18 shows the time-domain breathing pattern of a test person breathing normally. The signals are obtained at a distance of around 25 cm. For longer distances, the reflected signal decreases slightly in amplitude due to spreading loss, but the sweeping impulse correlation allows a determination of the signals with the same precision. Fig. 19 shows the breathing of a second test person, which is artificially fast and flat. Both breathing patterns are resolved clearly, with an abdomen deviation of more than 12 mm for normal breathing and around 8 mm for flat breathing.

Next, the breathing patterns of a seven-week-old infant are determined. In the first setting, the infant is sleeping in bed on its back. The sensor is mounted on a tripod as well here, pointing at the child's abdomen. In Fig. 20, a sequence of calm and rhythmic breathing is chosen for plotting. The abdomen deviation while breathing is larger than 1.5 mm.

In the second setting, the infant is sleeping in a typical car seat. A distance of around 20 cm is chosen between infant and sensor, as this is a distance where the sensor could be mounted on a typical handle of the car seat. The breathing plot is shown in Fig. 21. The breathing can be resolved very well in the car seat too. The measurement shows a sequence of arrhythmic breathing, very typical of infants; this needs to be taken into account when it comes to pattern recognition in a warning system. During arrhythmic breathing, the breathing is deeper, and therefore abdomen deviations of up to 3 mm can be determined.

V. Conclusion

In this paper, an assessment of IR-UWB technology for a precise movement determination and breath-rate sensing has been presented. The applied sweeping correlation method has been explained in detail, which is used to avoid sampling of the RF impulse with picosecond precision. The applied FCC-compliant hardware has been presented in detail, which consists of an IPG IC, generating a fifth Gaussian derivative

impulse, and a hardware correlator consisting of a monolithic correlator IC and an integrating BB circuit. The measurements qualify the circuits for use in the radar demonstrator. Using the proposed hardware, three methods of movement determination have been presented, from which the method of slope-to-slope tracking between direct coupling and object reflection is selected since it had the smallest error distribution. The presented measurements showed a movement precision in the millimeter to submillimeter range; this indicates that the method using sweeping impulse correlation is very well suited for precise position determination, movement detection, and breath-rate sensing. Breathing measurements on male humans and a seven-week-old infant have been presented. The proposed radar principle could be used for a detector and warning system, sensitive to a sleeping infant or child on the backseat of a car.

ACKNOWLEDGMENT

The authors would like to thank Dr. J. Dederer, now with Cassidian, Ulm, Germany, for the applied MMICs and Dr. M. Leib, now with Cassidian, Ulm, Germany, and Prof. Dr. W. Menzel, Institute of Microwave Techniques, Ulm University, Ulm, Germany, for the Vivaldi antenna. The authors would like to thank Dr. M. Fritzsche, Daimler AG, Ulm, Germany, for helpful discussions on child detection scenarios in automotives. The authors are indebted to the Si/SiGe foundry of Telefunken Semiconductors for the fabrication of the ICs.

REFERENCES

[1] C. McLaren, J. Null, and J. Quinn, "Heat stress from enclosed vehicles: Moderate ambient temperatures cause significant temperature rise in enclosed vehicles," *Pediatrics* vol. 116, no. 1, pp. e109–e112, Jul. 2005. [Online]. Available: http://www.pediatrics.org/cgi/content/full/116/1/e109 or http://ggweather.com/heat/index.htm

[2] "Revision of part 15 of the Commission's rules regarding ultra-wideband transmission systems," FCC, Washington, DC, USA, First Rep. and Order 02-48, Apr. 2002.

[3] T. E. McEwan, "Body monitoring and imaging apparatus and method," US. Patent 5 573 012, Nov. 16, 1996.

[4] M. Y. W. Chia, S. Leong, C. Sim, and K. Chan, "Through-wall UWB radar operating within FCC's mask for sensing heart beat and breathing rate," in *35th Eur. Microw. Conf.*, Paris, France, Oct. 2005, vol. 3, pp. 1–4.

[5] J. C. Y. Lai, Y. Xu, E. Gunawan, E. C.-P. Chua, A. Maskooki, Y. L. Guan, K.-S. Low, C. B. Soh, and C.-L. Poh, "Wireless sensing of human respiratory parameters by low-power ultrawideband impulse radio radar," *IEEE Trans. Instrum. Meas.*, vol. 60, no. 3, pp. 928–938, Mar. 2011.

[6] A. Lazaro, D. Girbau, and R. Villarino, "Analysis of vital signs monitoring using an IR-UWB radar," *Progr. Electromagn. Res.*, vol. 100, pp. 265–284, 2010.

[7] Y. Nijsure, W. P. Tay, E. Gunawan, F. Wen, Z. Yang, Y. L. Guan, and A. P. Chua, "An impulse radio ultra wideband system for contactless noninvasive respiratory monitoring," *IEEE Trans. Biomed. Eng.*, 2013, to be published.

[8] G. Ossberger, T. Buchegger, E. Schirmbäck, A. Stelzer, and R. Weigel, "Non-invasive respiratory movement detection and monitoring of hidden humans using ultra wideband pulse radar," in *Joint Int. UWB Syst. Workshop/UWB Syst. Technol. Conf.*, Kyoto, Japan, May 2004, pp. 395–399.

[9] A. Nezirovic, S. Tesfay, S. E. Valavan, and A. Yarovoy, "Experimental study on human breathing cross section using UWB impulse radar," in *Proc. 5th Eur. Radar Conf.*, Amsterdam, The Netherlands, Oct. 2008, pp. 1–4.

[10] B. Levitas and J. Matuzas, "UWB radar for breath detection," in *11th Int. Radar Symp.*, Vilnius, Lithuania, Jun. 2010, pp. 1–3.

[11] M. Leib, E. Schmitt, A. Gronau, J. Dederer, B. Schleicher, H. Schumacher, and W. Menzel, "A compact ultra-wideband radar for medical applications," *Frequenz*, vol. 63, no. 1–2, pp. 2–8, Jan./Feb. 2009.

[12] P. Devine, "Radar level measurement—The user's guide," VEGA Grieshaber KG, Schiltach, Germany, 2000.

[13] A. Schüppen, J. Berntgen, P. Maier, M. Tortschanoff, W. Kraus, and M. Averweg, "An 80 GHz SiGe production technology," *III-Vs Rev.*, vol. 14, no. 6, pp. 42–46, Aug. 2001.

[14] W. Sörgel, C. Waldschmidt, and W. Wiesbeck, "Transient responses of a Vivaldi antenna and a logarithmic periodic dipole array for ultra wideband communication," in *IEEE AP-S Int. Symp.*, Jun. 2003, vol. 3, pp. 592–595.

[15] B. Schleicher, J. Dederer, M. Leib, I. Nasr, A. Trasser, W. Menzel, and H. Schumacher, "Highly compact impulse UWB transmitter for high-resolution movement detection," in *IEEE Int. UWB Conf.*, Hannover, Germany, Sep. 2008, vol. 1, pp. 89–92.

[16] H. Sheng, P. Orlik, A. M. Haimovich, L. J. Cimini, and J. Zhang, "On the spectral and power requirements for ultra-wideband transmission," in *IEEE Int. Commun. Conf.*, Anchorage, AK, USA, May 2003, vol. 1, pp. 738–742.

[17] J. Dederer, A. Trasser, and H. Schumacher, "SiGe impulse generator for single-band ultra-wideband applications," in *Int. SiGe Technol. Device Meeting*, Princeton, NJ, USA, May 2006, pp. 274–275.

[18] J. Dederer, B. Schleicher, F. D. A. T. Santos, A. Trasser, and H. Schumacher, "FCC compliant 3.1–10.6 GHz UWB pulse radar system using correlation detection," in *IEEE MTT-S Int. Microw. Symp. Dig.*, Honolulu, HI, USA, Jun. 2007, pp. 1471–1474.

[19] J. Dederer, B. Schleicher, A. Trasser, T. Feger, and H. Schumacher, "A fully monolithic 3.1–10.6 GHz UWB Si/SiGe HBT impulse-UWB correlation receiver," in *IEEE Int. UWB Conf.*, Hannover, Germany, Sep. 2008, vol. 1, pp. 33–36.

[20] J. Dederer, A. Trasser, and H. Schumacher, "Compact SiGe HBT low noise amplifiers for 3.1–10.6 GHz ultra-wideband applications," in *Silicon Monolithic Integr. Circuits RF Syst. Top. Meeting*, San Diego, CA, USA, Jan. 2006, pp. 391–394.

[21] "AD9959—4-channel 500 MSPS DDS with 10-bit DACs," Analog Devices Inc., Norwood, MA, USA, Datasheet, Jul. 2005, rev. 0.

[22] "AD9959/PCB—Evaluation board for 4-channel 500 MSPS DDS with 10-bit DACs," Analog Devices Inc., Norwood, MA, USA, Datasheet, Oct. 2005, rev. 0.

[23] W. W. Macalpine and R. O. Schildknecht, "Coaxial resonators with helical inner conductor," *Proc. IRE*, vol. 47, no. 12, pp. 2099–2105, Dec. 1959.

[24] H. Koch, *Transistorsender: Entwurf, Berechnung und Bau von Sendern mit Transistoren*, 5th ed. Munich, Germany: Franzis, 1984.

[25] MEphisto Scope 1: Command-Interpreter. ver. Firmware 3.10, Meilhaus Electronic GmbH, Puchheim, Germany, Jan. 2010.

[26] LabWindows/CVI 8. ver. 8.0.0, National Instruments Corporation, Austin, TX, USA, 2005..

Bernd Schleicher (S'07–M'13) was born in Villingen-Schwenningen, Germany, in 1976. He received the Diplom-Ingenieur (FH) degree from Munich University of Applied Sciences, Munich, Germany, in 2004, and the Master of Science and Doctoral degrees from Ulm University, Ulm, Germany, in 2006 and 2011, respectively.

He is currently with TriQuint Semiconductor, Munich, Germany, where he is involved with power amplifier modules.

Dr. Schleicher was the recipient of the 2006 IHP Research Prize for his master thesis at the Institute of Electron Devices and Circuits, Ulm University. He was also the recipient of the 2010 EEEfCOM Innovations Prize for his work on a frequency modulated IR-UWB communication system.

Ismail Nasr (S'11) was born in Cairo, Egypt, in 1986. He received the Bachelor degree in electrical engineering from the German University of Cairo, New Cairo, Egypt, in 2008, and the Master of Science degree in microelectronics (with a focus on RF ICs) from Ulm University, Ulm, Germany, in 2010.

In 2006, he was as a Research Intern with Mentor Graphics, Cairo, Egypt. He is currently with the Institute for Electronics Engineering, Friedrich-Alexander-University, Erlangen–Nuremberg, Germany as a Research Assistant. His research interests include wideband RF and millimeter-wave ICs in silicon technologies for communication, radar, and dielectric spectroscopy.

Andreas Trasser received the Ph.D. degree from RWTH Aachen, Aachen, Germany, in 1989.

In 1990, he joined the Institute of Electron Devices and Circuits, Ulm University, Ulm, Germany, where he is currently a Member of the Academic Staff and a Lecturer. His research interests are mainly focused on the design of analog circuits.

Hermann Schumacher (M'93) received the Diplom-Ingenieur and Doktor-Ingenieur degrees from RWTH Aachen, Aachen, Germany, in 1982 and 1986, respectively.

From 1986 to 1990, he was with Bell Communication Research, Red Bank, NJ, USA, as a Member of Technical Staff. He then joined Ulm University, Ulm, Germany, as a Professor with the Institute of Electron Devices and Circuits, where, since 2010, he has been the Director. His research interests include compound semiconductor devices and their circuit applications. For over 15 years, his research group has focused on the application of Si/SiGe bipolar devices to microwave and millimeter-wave circuits and high-frequency microsystems. Lately the group has been especially involved with high data-rate millimeter-wave systems and impulse-radio UWB sensors. He has been a key player in large-scale national and European collaborative research projects, leading research consortia, and directing work packages in the areas on silicon–germanium heterostructure devices, RF, microwave and millimeter-wave ICs, RF microelectromechanical systems, and analog signal processing for gigabit/second wireless receivers. He is the Director of the Communications Technology International Master of Science Program of Ulm University (since 1998), past Vice-President for research (2000–2003), founder of the Competence Center on Integrated Circuits in Communications (in 2001, a public-private partnership), and, since 2011, Director of the School of Advanced Professional Studies, Ulm University, the university's continuing education arm.